ISSN 1064-2269, Journal of Communications Technology and Electronics, 2023, Vol. 68, No. 7, pp. 796–809. © Pleiades Publishing, Inc., 2023.
Russian Text © The Author(s), 2023, published in Radiotekhnika i Elektronika, 2023, Vol. 68, No. 7, pp. 703–717.

NOVEL RADIO SYSTEMS AND ELEMENTS

System of Laser Interferometers with a Large Spatial Difference to Study the Seismic-Deformation Oscillations of the Earth

M. N. Dubrov[a], *, I. A. Larionov[b], D. V. Alexandrov[a], and V. V. Kravtsov[a]

[a] *Kotelnikov Institute of Radioengineering and Electronics, Russian Academy of Sciences, Fryazino Branch, Fryazino, Moscow oblast, 141190 Russia*

[b] *Institute of Cosmophysical Research and Radio Wave Propagation, Russian Academy of Sciences, Far Eastern Branch, Paratunka Village, Kamchatka krai, 684034 Russia*

**e-mail: mnd139@ire216.msk.su*

Received December 23, 2021; revised January 26, 2022; accepted February 25, 2022

Abstract—The results of unique experiments on synchronous recording of oscillations of earth's surface with three laser interferometers–deformographs spaced at a distance of 6740 km, obtained during 2016–2020, are considered: two 100-m laser deformographs (Fryazino, Moscow oblast) and one 18-meter (Karymshina site, Kamchatka krai). It is shown that frequency-stabilized and thermocontrolled lasers, as well as systems for registering shifts of the compensation and modulation type interferogram provide an absolute instrumental resolution of 0.1–0.01 nm.

DOI: 10.1134/S1064226923070033

INTRODUCTION

Among the experimental methods and tools used for the study of geophysical processes, a special place is occupied by measuring systems with spatially spaced instruments. One of the important tasks of detecting and identifying seismic (acoustic) phenomena, which can be qualified, for example, as precursors or indicators of the processes of preparation and development of a major earthquake, is the ability of the system to emit a weak useful signal at the level of background natural and anthropogenic interference. These questions come to the fore when there is a problem of accurately determining the parameters of a weak earthquake or seismic event of artificial origin. Measurements of the deformation of a solid earth, such as expansion and contraction, inclinations and shifts of the earth's crust, are fundamental methods of research in geophysics since they provide primary information about the movements of the geological environment for scientific analysis. These instrumental methods [1–3] together with classical gravi-inertial seismic monitoring systems open up new possibilities of combined processing of simultaneous measurement of displacements and deformations of the earth in the seismic wave field [4, 5]. Improving the accuracy of seismic processes registration, the study of the nature and time dynamics of seismic-deformation wave fields become especially fruitful when using spatial separated systems of synchronously operating devices [6–9].

This paper presents the results of unique experiments, including synchronous registration of seismic-deformation oscillations of the earth's surface with three laser interferometers located at a distance of 6740 km from each other and installed in the aseismic (Moscow oblast) and seismically active (Kamchatka krai) zones. Preliminary results of the experiments were presented at the 11 International Conference STRPEP-2020 in Paratunka [10]. This publication provides a detailed description of the methods and tools used, as well as an extended analysis of the data recorded, and the results obtained.

1. LASER-INTERDIMENSIONAL INSTRUMENTS AND METHODS FOR MEASURING LINEAR AND SHEAR DEFORMATIONS

Wave disturbances excited by a source of any physical nature in a solid medium can be represented as a non-stationary vector field of spatial displacements ξ_k ($k = 1, 2, 3$) of medium particles. Displacements cause changes in pressure or deformation of the medium depending on its rheological, mechanical, and other physical properties.

The simplest problem of detecting an acoustic wave in a liquid or gas medium is solved by measuring the temporary changes in pressure at certain point x_k ($k = 1, 2, 3$) inside this medium using, for example, a microphone, a microbarograph, etc. A spatially distributed system of acoustic sensors is used to record the direction and coordinates of the source.

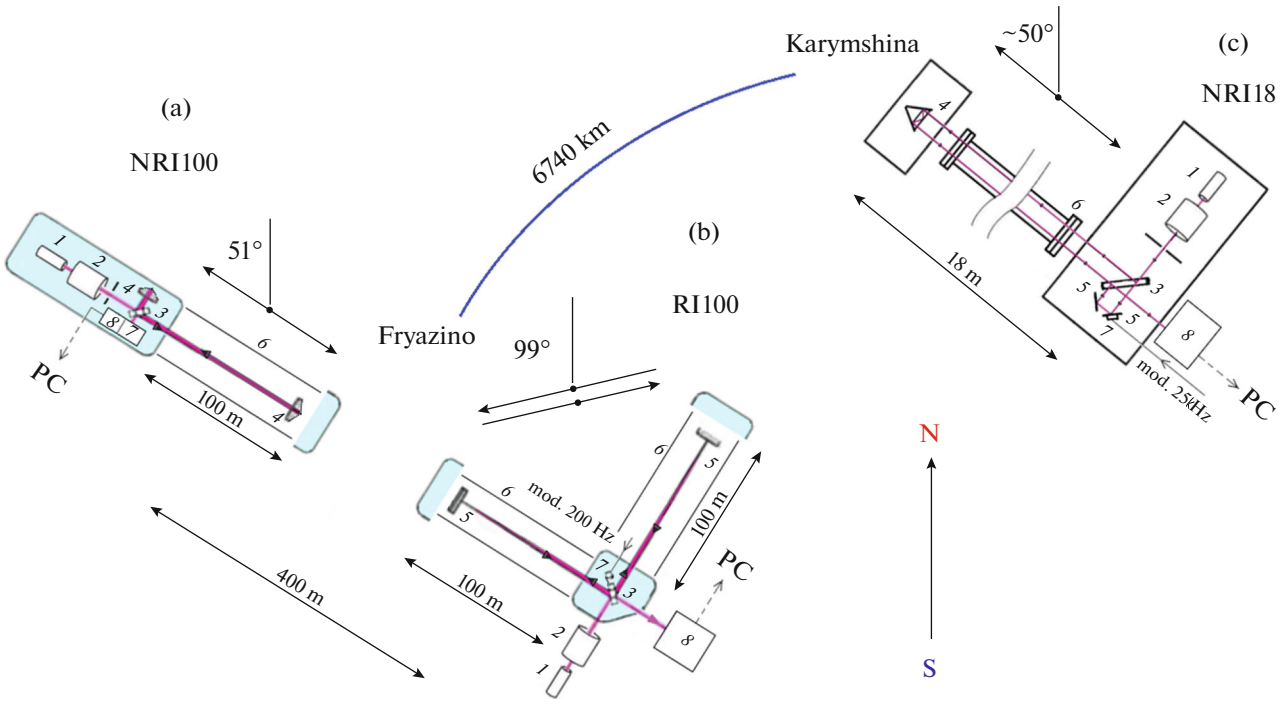

Fig. 1. Optical circuits and orientation in the space of un equal-arms (a, c) and equal-arms (b) interferometers–deformographs: (*1*) laser, (*2*) collimator, (*3*) light-splitting plate, (*4*) triple-prism reflector, (*5*) mirror, (*6*) protective tube, (*7*) mirror galvanometer or modulating electromechanical (piezo-ceramic) converter, (*8*) photoreceiver.

Other conditions occur in an elastic, solid environment. Equation of motion

$$\partial^2\xi_k/\partial t^2 = \chi\partial^2\xi_m/\partial x_k\partial x_m + q\partial^2\xi_k/\partial x_1^2 \quad (k,m = 1,2,3) \qquad (1)$$

in the left part contains the second time-derived component of the displacement vector of particles, and in the right, a combination of second space-derived displacements in a given plane, for example, $x_1 = 0$ (χ and q are dimensional combinations of Lamé constants and material parameters of the medium).

In seismology, the three components of the acceleration vector in the left part (1) are measured by accelerometers. A three-component sensor with a known pattern can determine the intensity of the wave and the azimuth of the source of the oscillation. Source localization is performed using longitudinal and transverse volume waves (so-called primary (P) and secondary (S) seismic waves). The amount of information received from a single sensor here increases in comparison with the acoustic sensing method.

Objective—Improving the efficiency of recording elastic waves in a solid medium: We use laser interferometers that measure the stresses (deformations) of the medium in the right side of Eq. (1), which are described by a second-rank tensor – six independent components. The number of registered parameters and equations for their calculation is also increasing.

Then, we use a multi-component laser strain gauge antenna, consisting of a system of spatially spaced laser interferometers [6, 8], which allows us to fully realize the advantages of the developed method of geophysical monitoring.

In this study, we use laser interferometers–deformographs that record changes in length Δl of the selected basis with length l, the relative linear deformation is defined as $\varepsilon = \Delta l/l$. Instruments with a length of 18 and 100 m are installed in two observation points, differing from each other in seismic and tectonic activity. Interferometers at the Fryazino Beam-Waveguide Site (underground beam-waveguide site) [10–15] are located in the aseismic zone of the Moscow syneclise [16]. The power of the sedimentary cover in the area of the landfill is 1400–1600 m, a large section of the crystalline foundation lowered to a depth of 3–4 km, the aulacogen near Moscow is located 20–30 km from the installation site of interferometers [10, 16]. A remote laser interferometer–deformograph works in a seismically active region in the tectonic fault zone off the eastern coast of Kamchatka [17, 18].

In experiments, two types of laser interferometers are used (Fig. 1). Unequal-arm interferometers (see Figs. 1a, 1b) measure the linear deformation, which determines the changes in the length of the large shoulder and is expressed in fractions of the laser wavelength. The equal-arm interferometer (see Fig. 1b), built according to the classical Michelson scheme, mea-

sures the difference of deformations in two mutually perpendicular directions, which corresponds to the transverse deformation of the shift parallel to the hypotenuse of the triangle formed by the shoulders of this interferometer.

At the Fryazino Beam-Waveguide Site (hereinafter, Fryazino Site) data were obtained using two 100-m instruments (see Figs. 1a and 1b), NRI100 unequal-arm interferometer [15] and RI100 equal-arm interferometer [11], the distance between them is 400 m. Lasers, optical, and electronic units are located underground at a depth of about 1.5–2 m. Light beams pass through an air-filled underground steel pipe, which is partly connected to the atmosphere.

An NRI18 18-m laser unequal-arm interferometer (see Fig. 1b) is installed on the surface of the earth on the Kamchatka Peninsula (Karymshina site of complex geophysical observations [17, 18]). The optical elements are mounted on casing pipes of two 5-m dry wells located at a distance of 18 m from each other. The optical path is shielded by a sealed pipe, which is protected from wind and precipitation by a special shelter.

Frequency-stabilized and temperature-controlled lasers with a wavelength of $\lambda = 632.8$ nm are used. In unequal-arm interferometers, residual frequency instability $\Delta\nu$ causes error in measuring deformations:

$$\varepsilon = \Delta l/l = \Delta\nu/\nu. \quad (2)$$

The relative long-term frequency instability of $\Delta\nu/\nu$ for the lasers used is $\sim 10^{-9}$ during hours and days. The short-term accuracy of the interferometer is improved in the thermal control schemes of the optical length of the laser and the interferometer [19]. The absence of forced modulation of the laser resonator reduces short-term (1–10 s) instability to 10^{-12} when installing devices in underground line conditions, which corresponds to a measurement error of 0.01–0.1 nm for interferometers with a length of 10–100 m. With such measured values, reverse optical scattering effects become important, which reduce the real accuracy of measurements by orders of magnitude. The limit on the level of optical feedback of the laser and interferometer is [20]

$$D_i G \ll K_i/t^2, \quad (3)$$

where $K_i = l_i/l$ is the ratio of laser lengths l_i and interferometer l, t is the transmittance of the laser mirror, G is the reflectance of the interferometer mirrors, representing the TEM_{00} amplitude of the wave, and D_i is the parameter of enhancing the feedback effect, dependent on laser frequency stabilization method [20].

The interferogram shifts are measured by a recording system (in three versions) that converts the length change of interferometer Δl into an electrical signal (Figs. 2a, 2b). Samples of these signals for instruments NRI100, RI100, and NRI18, their processing results, and examples of earthquake recording are shown in Figs. 3 and 4.

The NRI100 is equipped with a compensation recording system (see Fig. 2a), containing a transparent-reflective lattice (raster) as an interferogram position sensor and an actuator in the form of low-inertia mirror galvanometer *7*, moving the image of the interferogram along the raster [21]. Photoreceiver *8*, amplifier UPT *9*, and integrator *10*, connected to the mirror galvanometer, form an automatic control system with static and astatic links in the feedback circuit. The analog output is proportional to the offset of the interferogram, its period $\lambda/2 = 316.4$ nm is the calibration scale. The frequency range of this system model is limited from the top (~100 Hz), the record resolution is 0.01–0.001 nm in the 1 Hz band [22]. The dynamic range extension provides an automatic zero-point reference when the galvanometer mirror is deflected to the edge of the grid (Fig. 3a, curve *1*), the transfers are removed during processing (Fig. 3a, curve *2*; Fig. 4a).

In RI100 in the Fryazino Site (see Fig. 2b) a registration system of a modulation type is applied. Electromechanical modulator *7* is powered by a sinusoidal voltage of reference frequency *12*, *13* and generates an interference signal. Calculation of the phase difference within $0–2\pi$ and accounting for transitions through 2π is performed by a personal computer at the processing stage with a system resolution of 0.1–1 nm (Figs. 3b, 4b).

In the NRI18 registration system in the Karymshina Site (see Fig. 2b) to isolate the interference signal, piezoceramic modulator *7* is used, connected to a reference generator of sinusoidal voltage *12*, *13*. The phase difference between the reference (*12*, *13*) and measurement (*8*, *9*, *14*, *15*) channels is measured by phase detector *17* and the number of transitions through 2π is calculated on the PC as the difference between the measuring and reference counters (see Fig. 2c, *16* and *18* respectively). The basic accuracy of the recording system is $\lambda/4 = 158$ nm, or $\lambda/2 = 316$ nm, depending on the setting (Figs. 3c, 5g). The linearization of the phase detector output improves the system resolution to 0.1–1 nm.

To digitize the signals in the three described systems, 12–16-bit ADCs with a sampling frequency of up to 2 kHz are used, the results are received and accumulated in the PC.

In interferometers–deformographs with an air-filled protective tract, there are errors associated with changes in the refractive index of air, which are determined by the temperature, humidity, and pressure of the surrounding atmosphere. The contribution of the first two factors in thermostable underground premises is not significant, but variations in atmospheric pressure affect the operation of interferometers of any design [14, 23]. In this case, the U signal at the output of the laser interferometer registration system is expressed by ratio

$$U = A\Delta l + B\Delta p, \quad (4)$$

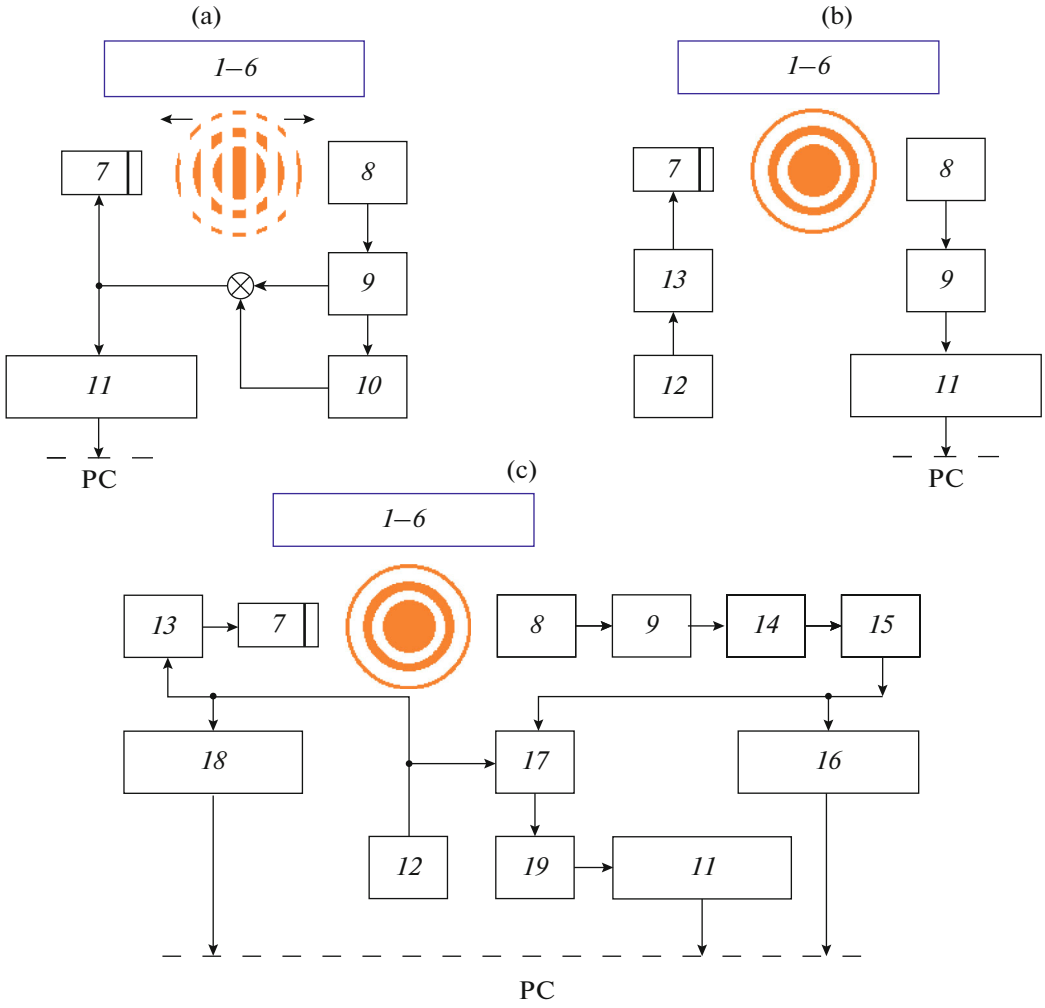

Fig. 2. Functional block diagrams of systems for registration of unequal-arms (a, c) and equal-arms (b) interferometers–deformographs: (*1–6*) elements of NRI100, RI100, and NRI18 interferometers (see Fig. 1), (*7*) modulator, (*8*) photoreceiver, (*9*) amplifier, (*10*) integrator, (*11*) ADC, (*12*) reference frequency, (*13*) modulating voltage generator, (*14*) band filter, (*15*) sine-meander converter, (*16*) measuring counter, (*17*) phase detector, (*18*) reference counter, (*19*) LF.

where Δl is the increment of the length of the deformograph, Δp is the variation of atmospheric pressure, coefficient A is the sensitivity of the interferometer to deformations, and B is its baric error. For example, for the NRI100 interferometer according to Fig. 3a, factor $a = 2 \times 10^3$ V/mm. Coefficient B according to the calculations [14] for the sealed interferometer varies between

$$B_1 = 3.6 \times 20 \text{ mV/mbar} = 72 \text{ mV/mbar}, \quad (5a)$$

and for free atmosphere,

$$B_2 = 72 \text{ V/mbar}. \quad (5b)$$

It is important to note that coefficient B_1 (5a) for an interferometer–deformograph with a sealed protective pipe decreases only by ~4 times (to $B_0 = 20$ mV/mbar) when it is replaced with a vacuum [23]. At the same time, with a partial connection of the measuring arm of the interferometer with the external atmosphere ($B_1 < B < B_2$) and measuring the deformation of the order of the tide in a solid earth $\varepsilon = \Delta l/l \sim 10^{-8}$–$10^{-7}$ both components in the ratio (4) become close in absolute value and the device equally effectively registers a linear combination of deformation of the earth's surface and variations in atmospheric pressure. This property of the interferometer–deformograph provides an interesting opportunity to study the features of deformation-baric processes and their relationship with geodynamic phenomena responsible for both the processes of preparation and development of large earthquakes [24, 25], and their impact on the earth's atmosphere [24, 26].

2. RESULTS OF SYNCHRONOUS SEISMIC OBSERVATIONS

Let us analyze the largest earthquakes simultaneously recorded by interferometers in the Moscow region and Kamchatka in 2016–2020 (Table 1).

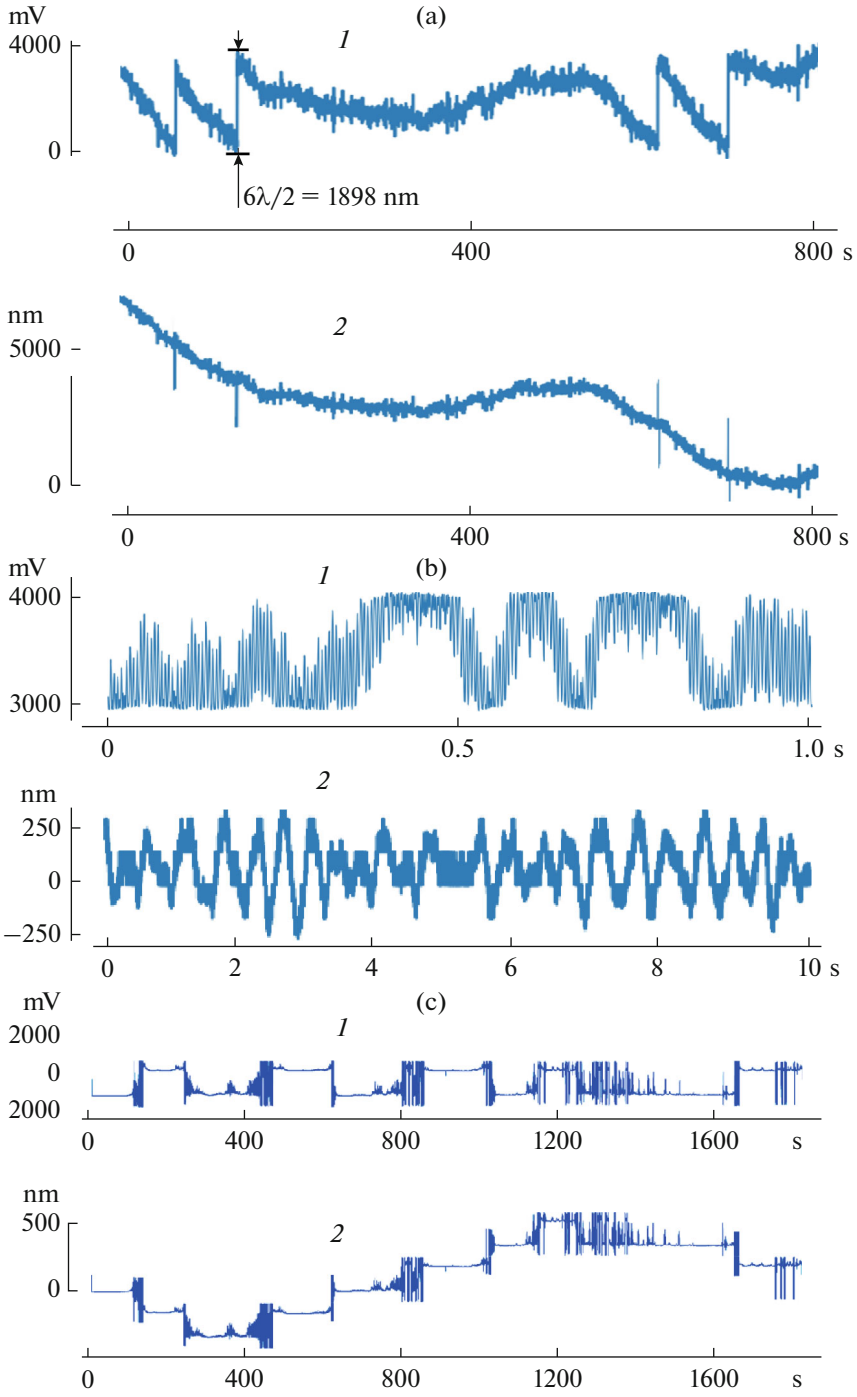

Fig. 3. Initial records of interference signals (*1*) in Fryazino for NRI100 (a) and RI100 (b), and in Karymshin for NRI18 (c); results of processing of the corresponding signals (*2*).

A feature of seismograms for interferometers and deformographs of any type is a slight amplitude of short-period volume P-waves in comparison with records of standard seismic channels [4]. The long-period surface waves of Rayleigh (R) and Liava (L) have large amplitudes and are recorded with interferometers with sufficient accuracy (Figs. 4a, 4c).

The amplitude of the deformation of the medium decreases with the increase in the length of the seismic wave directly proportional to the speed of its propagation in the medium [4, 6]. The velocities of volume P-waves are significantly higher than the velocities of the local microseisms, which makes it difficult to allocate P-waves against the background of

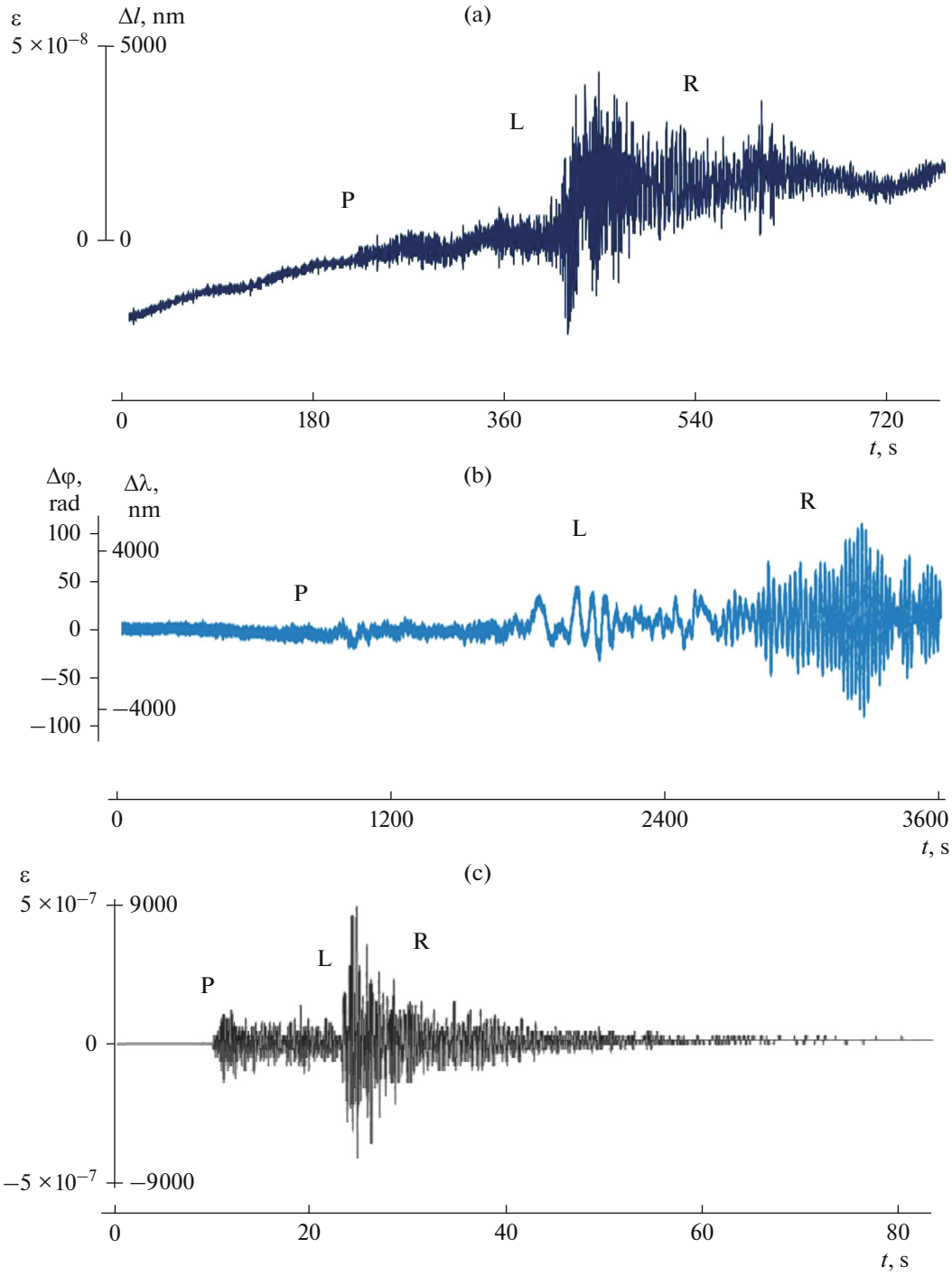

Fig. 4. Examples of remote earthquake detection: September 4, 2018, Urals, $m_b = 5.4$ (a), September 16, 2015, Chile, $M_w = 8.3$ (b) and local earthquake on March 14, 2016 off the East coast of Kamchatka, $M_p = 4.5$ (c).

interference. At the same time, volumetric teleseismic waves at the point of registration always have large exit angles [27], and therefore the interferometer with a horizontal arm, having a narrower directivity diagram [6, 11], is again in a less favorable situation compared to a standard pendulum-type seismometer. Therefore, the sensitivity and instrumental accuracy of instruments for measuring relative deformations $\varepsilon = \Delta l/l$ in the seismic wave field, when calculated on absolute displacements ξ_k of individual particles of the medium, should be comparable with the corresponding parameters of the standard seismic devices. To date, these conditions are being implemented in the most advanced laser-interferometric instruments and installations [1, 4, 5, 28].

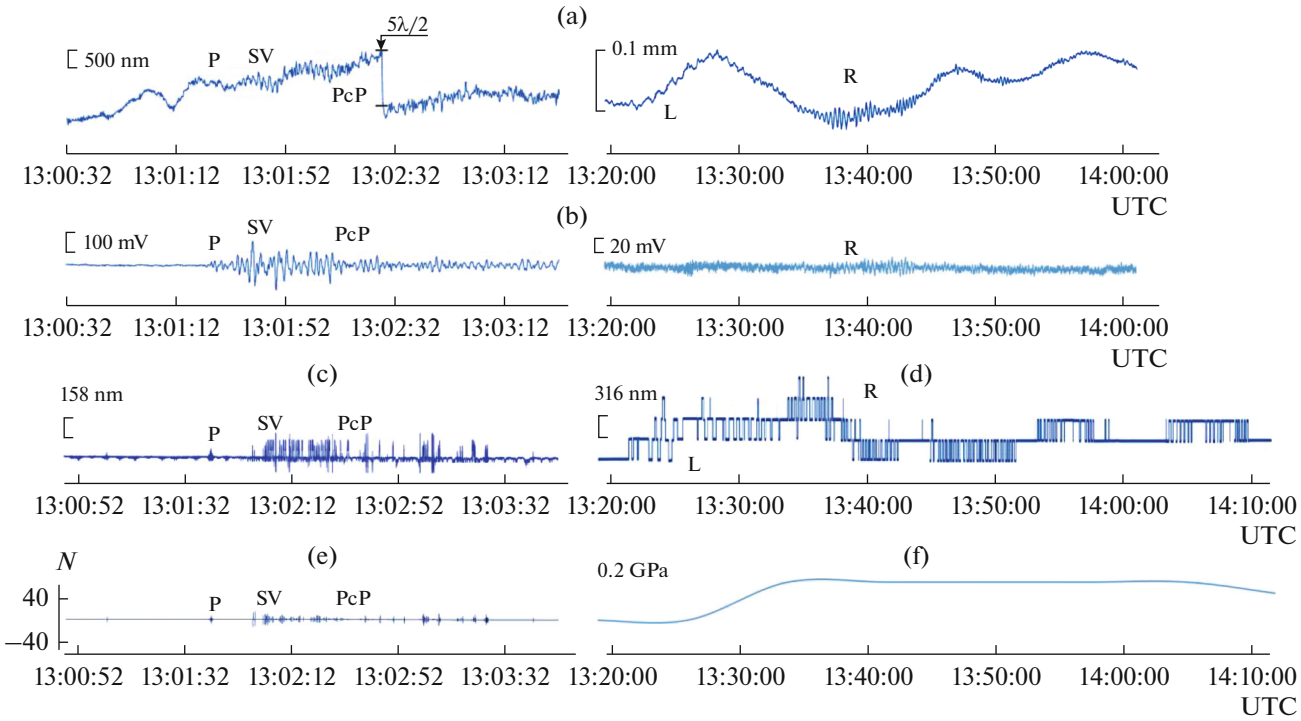

Fig. 5. Fragments of synchronous registration of the earthquake where $M_w = 7.8$ (south-west of Sumatra, 2016), made in Fryazino on the NRI100 (a) and vertical Z-component seismic receiver SNG-11 [29] (b) and Karymshina on the NRI18: The signal at the output of the phase detector (c), the difference in the readings of the measuring and reference meters in nm (d) and the units of the number of pulses (e), the variation of atmospheric pressure in Karymshina (f).

2.1. Registration and Allocation of Short-Period Volume P-Waves

Preliminary results of the March 2, 2016 earthquake (see Table 1) laser interferometers in the Karymshina and Fryazino sites are considered in our previous publications [10, 25]. Below, we give a more detailed analysis of the experimental material obtained and clarification of the results of detailed data processing.

Fragments of earthquake records are shown in Fig. 5. The first 3 min of recordings contain the introduction of the volumetric longitudinal P-wave. Recordings of long-period surface L- and R-waves for 30–40 min

Table 1. Data of the Unified Geophysical Service of the Russian Academy of Sciences (USGS) and the United States Geological Survey (USGS) on earthquakes

Date (UTC) yy-mm-dd	Time (USGS/ EGS), hh:mm:ss	Latitude (USGS/ EGS)	Longitude (USGS/ EGS)	Magnitude: M_w USGS/ M_s EGS	District (USGS/ EGS)
2016-03-02	12:49:48	4.95° S	94.3° E	M_w 7.8	Southwest of Sumatra, Indonesia
	12:49:46	4.78° S	94.26° E	M_s 7.5	
2017-09-08	04:49:19	15.0° N	93.9° W	M_w 8.2	101 km South of Tres Picos, Mexico
	04:49:19	15.0° N	93.69° W	M_s 8.3	Coast of Chiapas, Mexico
2020-01-28	19:10:24	19.42° N	78.8° W	M_w 7.7	The Caribbean Sea (NNW from Lucia, Jamaica)
	19:10:25	19.54° N	78.8° W	M_s 7.7	Region of Cuba (between Cuba and Jamaica)

See links: EGS—/www.ceme.gsras.ru/cgi-bin/new/catalog.pl; USGS—//earthquake.usgs.gov/earthquakes/.

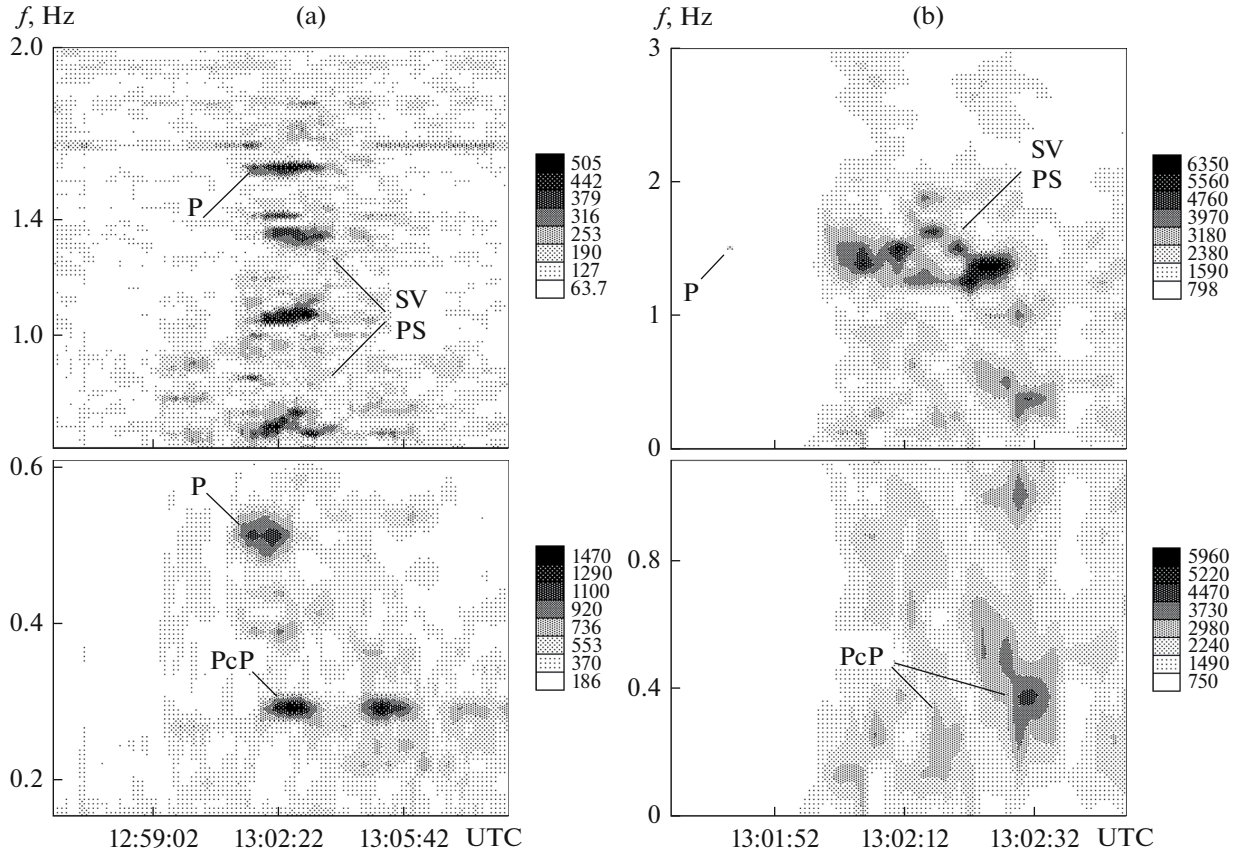

Fig. 6. Microstructure of spectral-time diagrams of arrival times and frequency ranges of volume P- and PcP-waves, as well as exchange PS- and SV-waves, highlighted in Fryazino (a) and Karymshina (b) after the earthquake of March 2, 2016, Sumatra. To the right of each graph is the time-frequency distribution for spectral brightness, its levels (relative units).

after the entry of the volume waves are given in the right columns of Figs. 5a, 5b, and 5d.

It turned out to be unexpected that the digital system of registration of the NRI18 interferometer in the Karymshina Site (see Figs. 5c and 5d), having less accuracy in conditions of low level of microseismic interference, due to its nonlinear properties, recorded the entry of volumetric waves with a greater sensitivity. Spectral-time analysis of the data allows you to more accurately determine the arrival times, microstructure, and frequencies of the emitted waves (Fig. 6).

Time synchronization of remote tools was carried out on radio signals of the exact time with an error of 1 s. Comparison of the results with the data of the nearest seismic stations, Obninsk (OBN) and Petropavlovsk-Kamchatsky (PET) of the Unified Geophysical Service, Russian Academy of Sciences, is presented in Table 2. The arrival times of the P-wave are consistent with these data and correspond to epicenter distances: As Δ increases, the time of the wave travel from the hypocenter to the point of registration increases proportionally. Estimates for average propagation speeds: 12.15 km/s (Fryazino) and 12.22 km/s (Karymshina) are consistent with the classical model of the Jeffries–Gutenberg Earth [30, 31] and coincide with the estimates of seismic data of the Obninsk and Petropavlovsk-Kamchatsky stations with an accuracy of 1.07 and 0.74%, respectively.

The spectral composition and temporal (phase) structure of the selected wave packets are interesting. P-waves recorded in the Fryazino Site at 13:01:25 UTC (see Fig. 5a), in the spectral-time diagram consists of several interfering components in the range of 0.52–1.58 Hz) (Fig. 6a). At the same time, three out of five components, 0.68, 1.06 and 1.36 Hz, appear with a delay of ~30 s relative to the P-wave containing two leading components of 0.52 and 1.58 Hz. The three lagging components can be interpreted as scattered SV- and PS-exchange waves [30, 31], excited by the main P-wave when it is reflected and passing through the boundaries of the interface, in this case, the near-Moscow aulacogen [16] at 20–30 km from the point of installation of the devices, as well as the Mohorovicic discontinuity, lying at a depth of ~45–48 km. In contrast to the bottom longitudinal P-wave, SV and PS-waves contain significant tangential components of the displacements of the earth's surface and are well recorded by horizontal interferometers. This is espe-

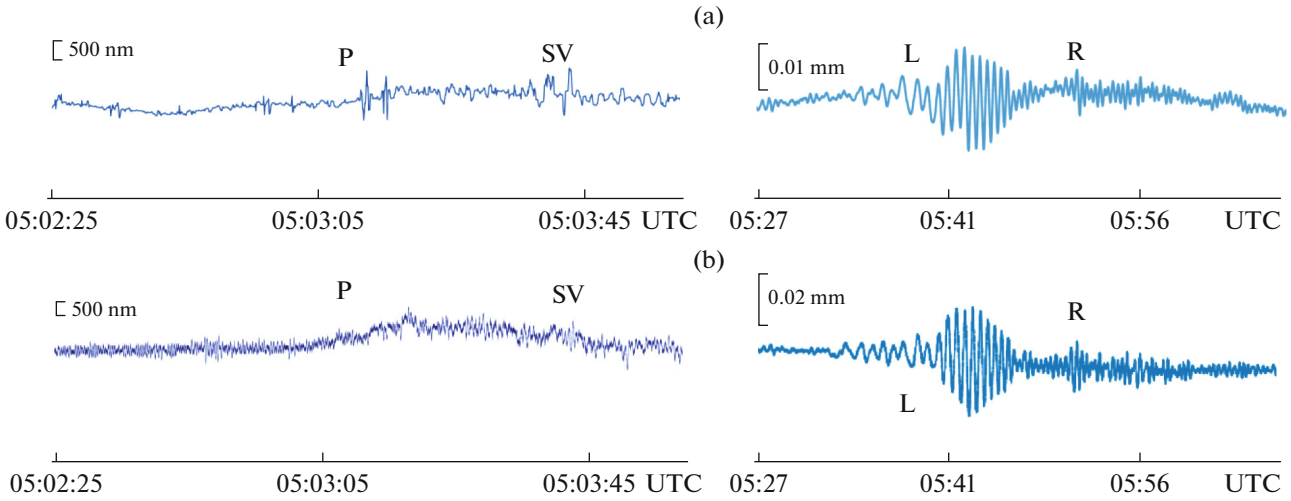

Fig. 7. Fragments of records of the earthquake where $M_w = 8.2$ (2017, Mexico), made by NRI100 (a) and RI100 (b) in Fryazino: Arrival of volume waves (left), registration of surface waves (right).

cially evident in the spectral-time diagram in the Karymshina Site (Fig. 6b). The phases of the SV- and PS-waves delayed by 20–40 s (group component in the region of 1.2–1.5 Hz) are six to eight times more intense than the main P-wave.

The spectral-temporal diagrams (see Figs. 6a, 6b) clearly distinguish lower-frequency PcP-wave phases reflected from the Earth's core [30, 31] with arrival times of 13:02:12 UTC (Fryazino site) and 13:02:30 UTC (Karymshina site), which are represented by spectral components in the region of 0.29 and 0.37 Hz. The possibility of separating these waves using the technique used is very interesting due to the fact that Jeffreys' hodographs for P- and PcP-branches at epicenter distances near $\Delta = 80°$ practically merge [30, 31].

A different situation is observed in the allocation of volumetric waves from the larger earthquake of $M_w = 8.2$ (Mexico September 8, 2017) (see Table 1). This powerful seismic event was recorded by NRI100 and RI100 Fryazino interferometers located at a distance of 0.4 km from each other [11, 15] (Fig. 7). Displacements Δl at the time of the arrival of the P-wave (05:02:51...52 UTC) do not exceed 100–200 nm for the NRI100 interferometer (see Fig. 7a) and are at the level of microseismic interference on the record of the RI100 interferometer (see Fig. 7b). This is explained by the magnitude of the epicenter distance of ~10 930 km ($\Delta \sim 98.5°$) for the Fryazino Site, which is located at the boundary of the shadow zone for both the direct P-wave and for reflected and scattered waves [30, 31]. As a result, both instruments detect interfering beams of weak diffracted waves of each of these types (see Figs. 7a, 7b).

Synchronous records of the earthquake of January 28, 2020 (Caribbean Sea), obtained by interferometers in the Fryazino and Karymshina sites are shown in Fig. 8. The time in the source, 19:10:24...25 UTC, is indicated by the vertical arrows. The epicenter distance to both points of observation is 1300–1600 km longer than for the earthquake off the coast of Sumatra in 2016 (see the beginning of this subsection), and the trajectory of the volume waves is respectively closer to the shadow zone. The estimated time of arrival of the P-wave on the recordings is indicated by vertical lines. Its arrival is almost indistinguishable in Fryazino in connection with the high level of the microseism (a), and to allocate the wave is possible considered above by the method of spectral-time analysis. The intro-

Table 2. The time of the arrival of the P-wave from the earthquake of March 2, 2016 (Southwest of Sumatra $M_w = 7.8/M_s = 7.5$; $t_0 = 12{:}49{:}48...46$ UTC) according to laser deformographs at Fryazino, Karymshina and seismic stations Obninsk and Petropavlovsk-Kamchatsky (www.ceme.gsras.ru/)

Site	Epicentral distance, km	Δ, deg	Arrival time (UTC), hh:mm:ss	Run time
Fryazino	8470	76.31	13:01:25	11 m 37 s
Karymshina	8740	78.74	13:01:45	11 m 57 s
Obninsk	8510	76.67	13:01:35.8	11 m 48 s
Petropavlovsk-Kamchatsky	8760	78.92	13:01:50.4	12 m 02 s

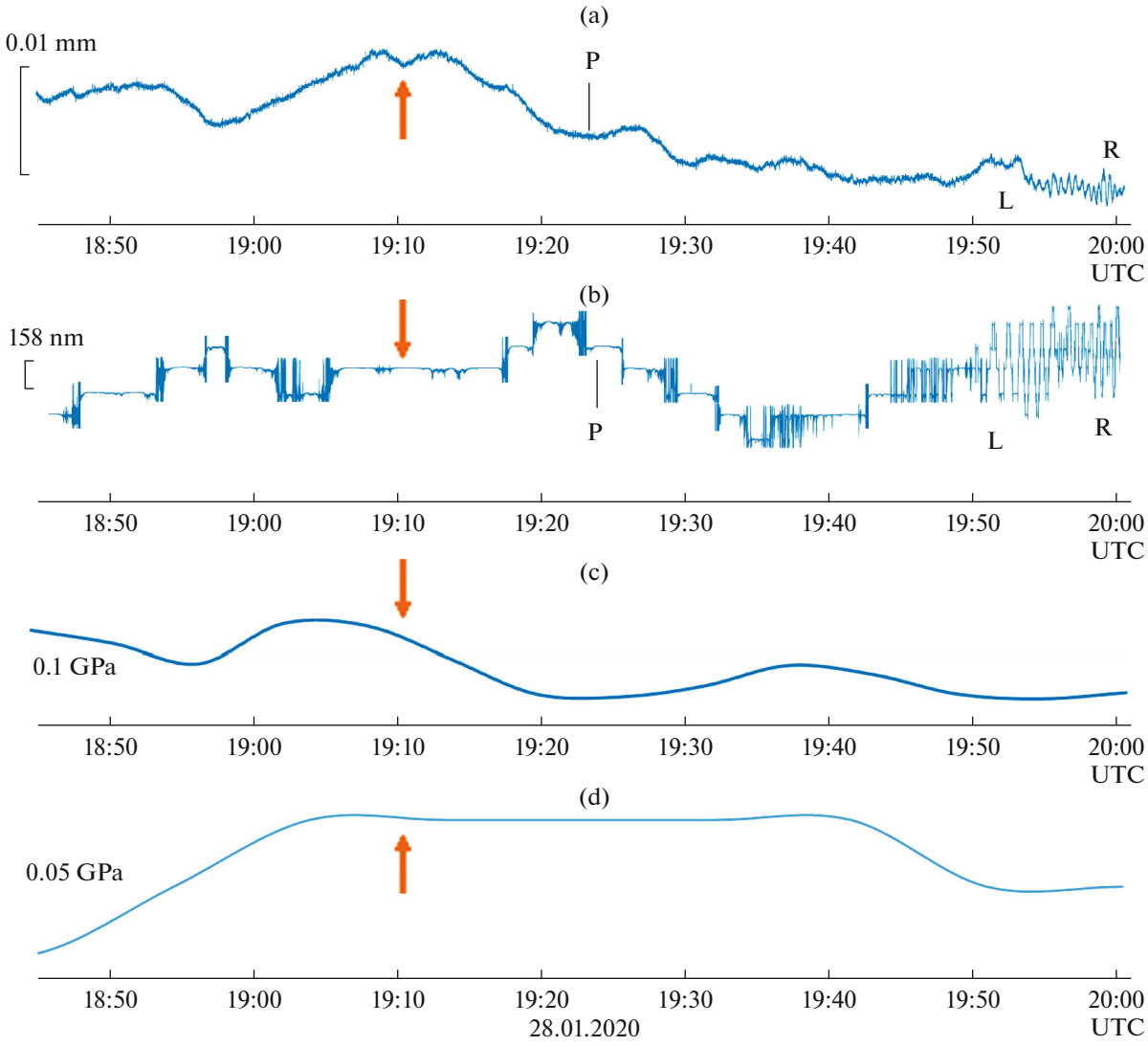

Fig. 8. Synchronous recordings of the earthquake where $M_w = 7.7$ (2020, Caribbean), made by NRI100 (a) and NRI18 (b) and variations in atmospheric pressure, respectively in Fryazino (c) and Karymshina (d).

duction of a P-wave in Karymshina falls on a nonlinear section of the characteristics of the registration system with a small value of conversion coefficient A (see formula (4)), and the amplitude of the measured oscillations becomes less than the resolution of the registration system 1–0.1 nm, which on an 18-m base corresponds to the magnitude of relative deformations of the order

$$\varepsilon = \Delta l/l \sim 10^{-10} \ldots 10^{-11}.$$

2.2. Low-Frequency and Ultra-Low-Frequency Seismic Deformation Oscillations

The results of recording low-frequency (long-period) waves from the earthquakes in question (see Table 1) shown in the right-hand columns in Figs. 5a–5g and 7, in the right-hand parts of Figs. 8a, 8b, and 9.

Surface waves in Fryazino and Karymshina (see Figs. 5a, 5d) for the highest amplitude of the wave trains have characteristic periods of 40–50 s (L-waves) and 15–25 s (R-waves). The Basic Accuracy and Recording Scale in Fig. 5g is expressed in units of $\lambda/2 = 316$ nm. The surface transverse L-wave does not contain a vertical displacement component and is not present on the seismic Z-channel record (see Fig. 5b on the right). The R-wave, containing vertical and horizontal components, on this record has a noticeable although insignificant amplitude due to a sharp drop in the amplitude-frequency characteristic of the seismic channel in the range of periods greater than 10 s (the intrinsic frequency of pendulum SNG-11 is 5 Hz [29]). The time of arrival of the most intense L- and R-wave trains in Fryazino and Karymshina are respectively 13:23:30...50 and 13:37:10...40 UTC. Taking into account the epicenter distances of each item

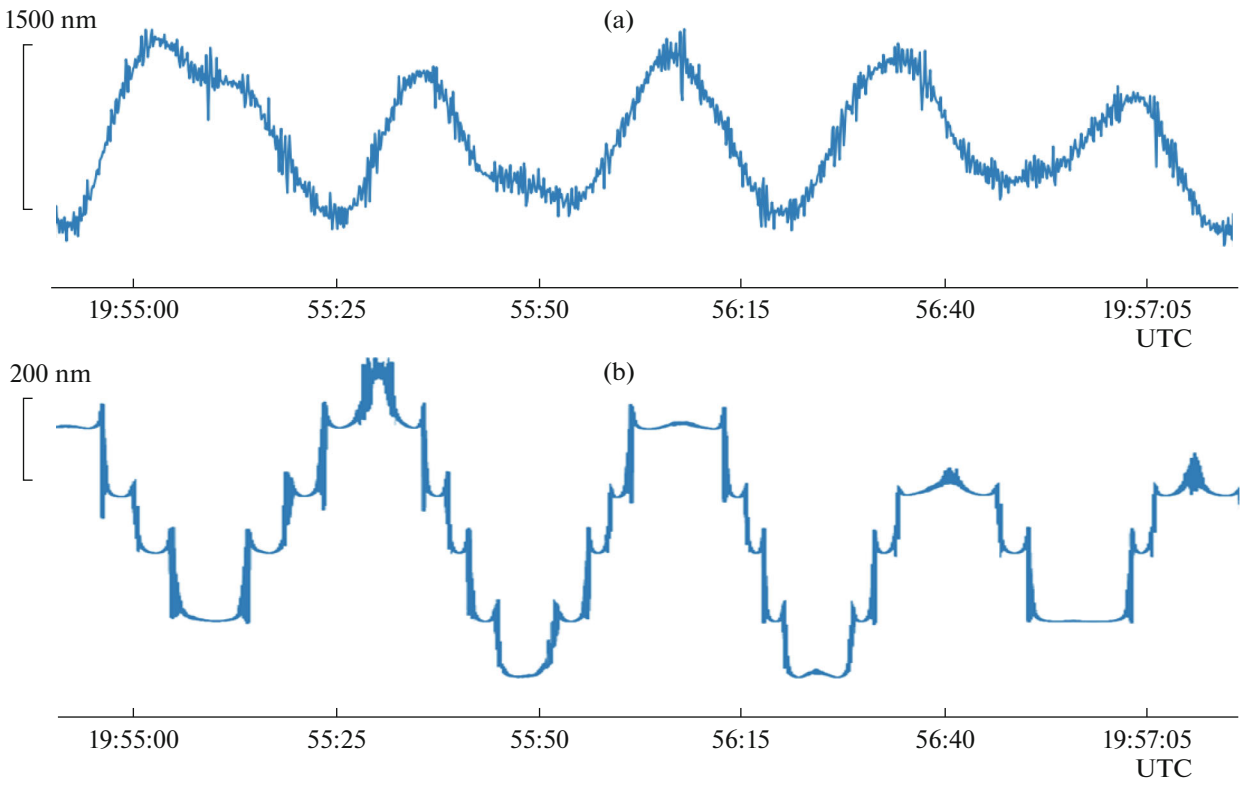

Fig. 9. Synchronous recordings of surface waves caused by the $M_w = 7.7$ earthquake (January 28, 2020): Registration by the NRI100 interferometer in Fryazino (a), registration by the NRI18 interferometer in Karymshina, basic accuracy $\lambda/4 = 158$ nm (b).

(see Table 2) estimates of the average propagation speeds of these waves are obtained: $V_L = 4.17–4.30$ km/s and $V_R = 2.96–3.06$ km/s, which agree well with the values of group velocities of L- and R-waves by independent seismic and strain-metric measurements [31, 32].

A comparison of the surface L- and R-waves from the Mexican earthquake where $M_w = 8.2$ on September 8, 2017, recorded by two interferometers at the Fryazino radial range, is given in the right part of Fig. 7. Maximum L-wave amplitudes for the RI100 interferometer (Fig. 7b on the right) at 05:42 UTC reach a value of 20.2 microns. This is about twice the maximum amplitude of L-waves of 10.5 microns on the recording of the interferometer NRI100 (Fig. 7a left). The estimated amplitude ratio for the directivity diagrams of the RI100 and NRI100 interferometers in the transverse wave field is 2 : 1 [6, 11], which corresponds with an accuracy of ~4% to the experimentally obtained value.

Surface L- and R-waves from the earthquake where $M_w = 7.7$ in the Caribbean Sea on January 28, 2020, recorded in Fryazino and Karymshina from 19:40 to 20:00 UTC are completely different (see Figs. 8a and 8b). Although the difference in epicenter distances for these points is only a few percent, wave trains differ at the time of their maximum amplitudes at 19:55–19:58 UTC (Fig. 9): characteristic periods of fluctuations in Fryazino and Karymshina—30 and 35 s, respectively. This is due to the difference in the phase velocities of these waves [31] and the geology of the medium on the path of their propagation: The signal from the Caribbean comes to Fryazino across the Atlantic and the western part of Eurasia, while in Karymshina the wave passes along the sides of the Pacific and North American tectonic plates.

Except for the standard long-wave L- and R-waves in Figs. 5 and 8 see special ultra-long-period (ultra-low-frequency) oscillations with characteristic periods of 10–40 min. The amplitude of these oscillations is three to four times greater than the amplitude of L- and R-waves, which indicates their possible baric origin. To date, we have accumulated experience that indicates the connection of the observed deformation-baric processes with the activity of tropical cyclones in the oceans, often preceding strong earthquakes and acting here as their trigger mechanism [25, 33].

The earthquake of March 2, 2016 (Sumatra, $M_w = 7.8$) can be associated with the development of the powerful tropical cyclone Winston (highest category 5 SSHWS) in the South Pacific in February 2016 and the completion of its activity on March 3, 2016 off the coast of Australia. The Caribbean earthquake on January 28, 2020 (see Fig. 8) on the border of the North and South American plates is accompanied by a very

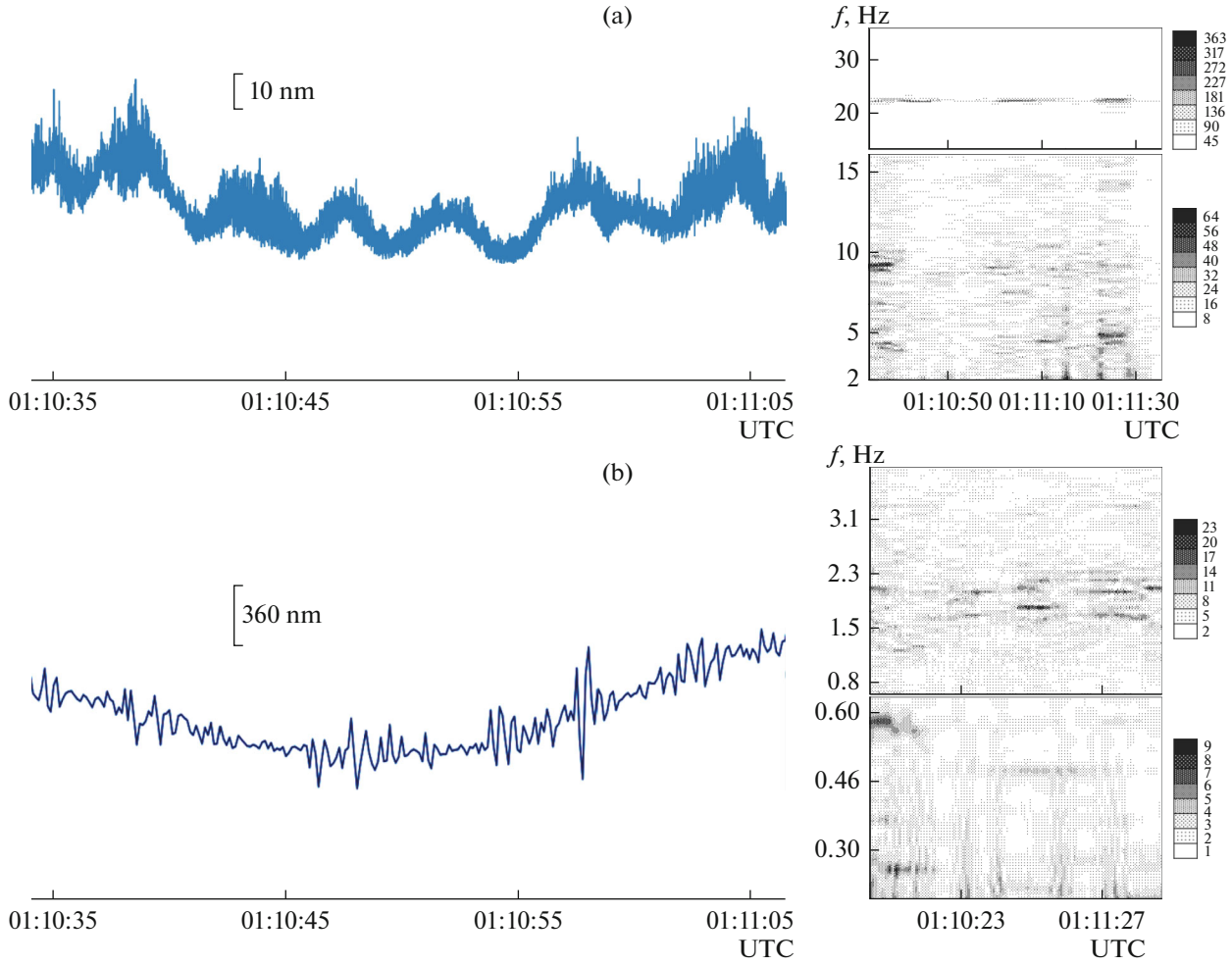

Fig. 10. Synchronous recordings of microseismic deformations and their spectral-time diagrams obtained in Karymshina (a) and Fryazino (b) on January 28, 2020.

rare phenomenon, the development of the subtropical cyclone Kurumi off the coast of Brazil (South Atlantic) from January 22–26, 2020, and its accelerated movement across the boundary of the plate section toward the African tectonic plate.

For both earthquakes (Figs. 5, 8) there is a correlation of the ultra-long-period oscillations recorded in Fryazino and Karymshina with a characteristic delay of 7–8 min. Confirmation of the baric origin of the detected waves is the correlation of the signals of laser interferometers–deformographs and variations in atmospheric pressure (Figs. 5f, 8c, 8d). Estimates of strain-baric coefficient B (4) for both instruments in relative units vary within $1–3 \times 10^{-7}$ GPa^{-1}.

2.3. Study of Synchronous Recordings of Microseismic Deformations

Microseisms continuously and everywhere excite the earth's crust in the frequency range from 10^{-2} to 10^{2} Hz. In a range of periods of more than 1 s, they are caused by oceanic surf, wind, and large meteorological disturbances in the oceans. Microseisms in the frequency range above 1 Hz are usually excited by technogenic sources and form spatially distributed partially coherent seismic fields. The study of the properties and behavior of broadband microseismic oscillations is considered as a possible method for studying the precursors of earthquakes [13, 25, 34].

The laser interferometer allows you to examine the characteristics of the microseism in wide ranges of frequencies and amplitudes. At the same time, the system of spatially spaced laser interferometers is able to determine the coherent properties of detected microseismic fields. During 2016–2020, laser interferometers in Fryazino and Karymshina performed several sessions of synchronous measurement of microseismic deformations. Examples of analysis of data obtained 18 h before the $M_w = 7.7$ earthquake in the Caribbean Sea (see Table 1), shown in Fig. 10.

The registration system of the NRI18 interferometer (Karymshina) in linear mode records 4–6 s storm microseisms (see Fig. 10a left). Their relatively large amplitude of 10–20 nm is explained by the proximity

(30–40 km) of the surf on the Pacific coast. The usual amplitudes of 4–6 s of storm microseisms from the Atlantic, recorded in the Moscow region (1000–1200 km to the oceanic coast) are units of nanometers for a laser interferometer of the same length, installed in a deep tunnel [3]. Synchronously working 100-m interferometers in Fryazino records 0.3–0.4 s of technogenic microseisms (see Fig. 10b on the left). Their amplitudes increase to 200–300 nm during the day and decrease several times during the night period.

The results of the spectral-temporal analysis of high-frequency microseisms are shown in (Fig. 10 right). In Karymshina (see Fig. 10a, right), the peaks at 4.5, 9.1, and 14 Hz are highlighted. The narrow and intense peak of 22 Hz is quite coherent and is due to the resonant properties of the device design. On the spectrograms of the interferometer in Fryazino (see Fig. 10b right), the following peaks are detected: 0.27, 0.49, and 0.59 Hz. The split spectral peak at a frequency of about 1.9 Hz is isolated at the top of the spectrogram in Fig. 10b and shows here moderate coherent properties. It should be noted that the strong splitting of this spectral peak was observed using the same 100-m laser deformograph before the large $M_w = 8.3$ earthquake in Chile on September 16, 2015 [25].

CONCLUSIONS

The results of unique experiments on synchronous registration of seismic deformation oscillations of the Earth's surface with three laser interferometers with measuring bases of 18–100 m, spaced at a distance of 6740 km. The methods used and the results achieved, according to the data published to date, are original and obtained for the first time.

Used as radiation sources, frequency-stabilized and thermocontrolled lasers together with recording systems of compensation and modulation types, measuring interferogram shifts, provide an absolute instrumental resolution of 0.1–0.01 nm on interferometric bases up to 100 m.

The effectiveness of the proposed methods is demonstrated by the examples of the registration of remote earthquakes $M_w = 7.7–8.2$ and the isolation of volume and surface waves used in seismology. The results of spectral analysis of data obtained in the sessions of synchronous observations during 2016–2020 were compared with the data of regional and global seismic services. The development of the proposed methods can be useful for the detection and identification of precursors of major seismic events and other natural hazards.

FUNDING

The work was supported by the state tasks of the Kotelnikov Institute of Radioengineering and Electronics, Russian Academy of Science, project no. 0030-2019-0014 and Institute of Cosmophysical Researches and Radio Wave Propagation, Russian Academy of Science, project no. AAAA-A21-121011290003-0.

CONFLICTS OF INTEREST

The authors declare that they have no conflicts of interest.

REFERENCES

1. S. Takemoto, H. Momose, A. Araya, et al., J. Geodynamics **41** (1-3), 23 (2006).
2. A. Amoruso and L. Crescentini, J. Geodynamics **48** (3-5), 120 (2009).
3. V. A. Volkov and M. N. Dubrov, Marees Terrestres Bull. d'Informations **BIM—148**, 11971 (2014).
4. A. V. Nikolaev, A. V. Lukanenkov, and M. N. Dubrov, Doklady / Earth Science Section **430/2**, 258 (2010).
5. A. J. Barbour and D. C. Agnew, Bull. Seismological Soc. Amer. **102** (6), 2484 (2012).
6. M. N. Dubrov and R. F. Matveev, J. Commun. Technol. Electron. **43**, 1068 (1998).
7. P. Spudich and J. B. Fletcher, Bull. Seismological Soc. Amer. **98** (4), 1898 (2008).
8. M. N. Dubrov and D. V. Aleksandrov, in *Proc. 6th Int. Conf. Antenna Theory and Techniques, Sevastopol, 17–21 Sep. 2007* (IEEE, New York, 2007).
9. G. I. Dolgikh, Tech. Phys. Lett. **44**, 923 (2018).
10. D. Aleksandrov, M. Dubrov, V. Kravtsov, and I. Larionov, in *Proc. 11 Int. Conf. Solar-Terrestrial Relations and Physics of Earthquake Precursors. Paratunka, 22–25, Oct. 2020.* Ser. E3S Web of Conf. V. 196. Les Ulis: EDP Sci. 2020, Article No. 02010.
11. M. N. Dubrov and R. M. Karmaleeva, Izv. AN SSSR. Fiz. Zemli, No. **7**, 81 (1976).
12. V. P. Vard'ya, M. N. Dubrov, I. P. Korshunov, and R. F. Matveev, Radiotekh. Elektron. (Moscow) **23**, 2068 (1978).
13. M. N. Dubrov and V. A. Alyoshin, Tectonophysics **202** (2-4), 209 (1992).
14. M. N. Dubrov, L. A. Latynina, R. F. Matveev, A. V. Ponomarev, Fiz. Zemli, No. 12, 22 (1998).
15. D. V. Aleksandrov, M. N. Dubrov, V. V. Kravtsov, Nelin. Mir. **16** (2), 44 (2018).
16. N. N. Kolosova and E. A. Churilova, *Atlas of the Moscow Region* (Prosveshchenie, Moscow, 2004), p. 11.
17. I. A. Larionov and Yu. A. Nepomnyashchii, Vestn. KRAUNTs. Fiz.-Mat. Nauki, No. 3, 85 (2016).
18. Yu. V. Marapulets, O. P. Rulenko, I. A. Larionov, and M. A. Mishchenko, Doklady / Earth Science Section **440/1**, 1349 (2011).
19. M. N. Dubrov, "The device for measurement of movements and deformations of objects," RF Patent No. 2336495, Ofits. Byul. "Izobreteniya. Poleznye Modeli," No. 29, (20.10.2008).
20. M. N. Dubrov, *Long Basic Llaser Interferometry: Accounting of the Return Dispersion* (MFTI, Moscow, 2011).

21. M. N. Dubrov, "The watching system for optical interferometers," Patent SSSR No. 720292, Ofits. Byul. "Izobreteniya," No. 9 (05. 03.1980).
22. M. N. Dubrov and P. V. Medvedev, in *Proc. 4th Int. Conf. on Advanced Optoelectronics and Lasers, Alushta, Sep. 29–Oct. 4, 2008* (IEEE, New York, 2008).
23. D. Berger and R. Lovberg, Prib. dlya Nauch. Issled. **40** (12), 41 (1969).
24. M. N. Dubrov and V. M. Smirnov, Geomagn. Aeron. **53** (1), 49 (2013).
25. D. V. Aleksandrov, M. N. Dubrov, I. A. Larionov, et al., J. Volcanol. Seismol. **13**, 193 (2019).
26. V. I. Zakharov, V. A. Pilipenko, V. A. Grushin, and A. F. Khamidullin, Solnechno-Zemnaya Fiz. **5** (2), 114 (2019).
27. G. P. Avetisov, *Geophysical Methods of Prospecting in the Arctic* (NIIGA, Leningrad, 1974), No. 9, p. 96.
28. V. M. Loborev, S. F. Pertsev, V. V. Sudakov, et al., *Physics of Nuclear Explosion,* Vol. 5: *Control of Nuclear Tests* (Fizmatlit, Moscow, 2017), p. 161.
29. SNG-11D/GSC-11D/OPEN. Prospekt Firmy Geo-Spase, Houston, 2006. https://ds.iris.edu/ds/nrl/sensor/geospace/gs-11d/.
30. H. Jeffreys, *The Earth, its origin, hystory and physical constitution* (Cambridge Univ. Press, Cambridge, 1959; Inostrannaya Literatura, Moscow, 1960)
31. V. N. Zharkov, *Internal Structure of Earth and Planets* (Nauka, Moscow, 1983).
32. R. M. Karmaleyeva, L. A. Latynina, and E. F. Savarensky, Pure and Appl. Geophys. **82** (1), 85 (1970).
33. V. Volkov, J. Mrlina, M. Dubrov, et al., Geodz. Geodnm. **11**, 442 (2020).
34. G. A. Sobolev, Natural Hazards Earth Syst. Sci. **11** (2), 445 (2011).